Statistical characterization of thermally evaporated rough CaF_2 films

D. R. Luhman and R. B. Hallock

Laboratory of Low Temperature Physics, Department of Physics, University of Massachusetts, Amherst, Massachusetts 01003, USA

(Received 14 May 2004; revised manuscript received 2 July 2004; published 19 November 2004)

Thermal deposition of CaF_2 onto a glass substrate creates a nanoscale rough surface. A series of samples with differing nominal CaF_2 film thicknesses have been fabricated, and the topography has been investigated using atomic force microscopy. Measured values for the statistical characterization of the samples are presented including the exponents describing the scaling behavior of the surfaces. We find that the roughness exponent $\alpha=0.88\pm0.03$, the growth exponent $\beta=0.75\pm0.03$, and the dynamical exponent $z=\alpha/\beta=1.17\pm0.06$. We also measure the multifractal spectra and nearest neighbor height difference probability distribution. The results are consistent with noise dominated by a power-law distribution with exponent $\mu+1\approx4.6$. Profilometer measurements were used to determine the porosity ϕ of the deposited films, which we find to be constant for all film thicknesses with $\phi\approx0.46$.

DOI: 10.1103/PhysRevE.70.051606 PACS number(s): 68.35.Ct, 68.55.Jk, 68.55.Ac, 81.15.Ef

I. INTRODUCTION

Rough calcium fluoride has been used extensively as a substrate to create rough metallic surfaces that have been studied using surface plasmon techniques [1–5]. Several of those studies have investigated how the roughness of the metallic surface changes with different thicknesses of CaF_2 [3,4,6]. Other authors have measured surface roughness as a function of CaF_2 thickness for both metallic coated and uncoated CaF_2 surfaces using a replication technique followed by a microdensitometer analysis of the impression [7,8]. One purpose of the present work is to characterize deposited CaF_2 films on glass as a function of coverage using atomic force microscopy (AFM) and profilometer measurements. We are not interested in the optical properties of metals deposited on these surfaces, but rather our interest is in using the surfaces themselves as an adsorption substrate for ^{4}He thin films. This makes the roughness characteristics of the surfaces produced of direct interest. The results of measurements on two sets of substrates spanning similar thickness regimes are reported here. The first set, referred to as I, contains substrates made solely for the purpose of surface analysis. The second set (II) is comprised of samples that were used for a ^{4}He thin film adsorption study after which the surface structure of the substrates was examined. A separate report will provide the details of the low temperature experiments studying ^{4}He adsorption and sound modes of the adsorbed ^{4}He films [9]. Data were also collected on a third set (III) of substrates spanning a more limited thickness regime and consisting of CaF_2 deposited on gold plated glass.

In addition to the characterization of the CaF_2 films for ^{4}He adsorption studies, we present an analysis of the AFM images that show the scaling behavior of the surfaces. The subject of nonequilibrium surface growth and the kinetic roughening of surfaces is of considerable interest. Many studies including theoretical work, numerical simulations, and experiments have contributed to the subject of dynamical scaling of growing interfaces and involved a variety of systems. A number of different models have been proposed that incorporate different combinations of processes that may be relevant during the growth of the surface. In many cases the scaling exponents, which characterize each universality class, can be determined by solving the governing stochastic growth equations exactly or by numerical simulation. By preparing thin films of varying thicknesses on flat substrates the scaling behavior of the surfaces can be observed experimentally in $2+1$ dimensions. Several reviews have been written on this subject [10–13].

From our measurements and analysis we report obtained values for the roughness exponent α, the growth exponent β, and the dynamical exponent $z=\alpha/\beta$ for a range of nominal thicknesses of CaF_2 deposited on glass. We interpret these results as evidence for the existence of power-law-distributed noise in our samples, which indicates nonuniversal behavior. Prior to this report a brief mention of the fractality of thin CaF_2 films was made in the literature, but the results were inconclusive [14]. We observe that our surfaces indeed exhibit multifractality. We have previously reported on the multifractality and power-law distributed noise in this system [15]. The purpose of the current paper is to thoroughly report on our characterization of the roughness of vacuum deposited CaF_2 surfaces.

CaF_2 was chosen for this study because it can be easily deposited and patterned on substrates, and is thus suitable for our ^{4}He film experiments. In Sec. II we discuss sample fabrication, the imaging procedure and height profile measurements. Sections III and IV consist of results derived from the AFM and profilometer measurements. Section III outlines an analysis of the surfaces similar to what has been done previously in this group [16,17] and by others, which allows for comparison. This includes the calculation of length scales, which are said to be characteristic of the surface structure. Section IV, on the other hand, presents the same AFM data analyzed within the dynamical scaling framework. Concluding remarks are presented in Sec. V.

II. EXPERIMENTAL DETAILS

A. Sample fabrication

All samples were fabricated using the same protocol; the only differences were the amount of CaF_2 deposited and additional depositions of Ag and Al on the substrates in set II, which were used during the low temperature experiments at $T=1.671$ K [9]. The samples in set II were glass microscope slides cut to 4.45×2.54 cm. Before each evaporation the glass substrates were mounted in the bell jar and the pressure was reduced to ~30 mT and a 1.5-kV ion etch was applied for 10 min. The pressure in the bell jar was then reduced to ~5 μT, and the material was deposited. First, silver and aluminum were selectively deposited to function as drivers and detectors for the helium sound modes. Specifically, 50 nm of silver was vacuum deposited to act as electrical contact pads, followed by 0.15-mm$\times$2.0-cm$\times$30-nm silver strips which function as sound drivers. Similar aluminum strips were then deposited to form transition edge superconducting detectors. The silver and aluminum depositions were from tungsten wire basket sources at a rate of 0.5 nm/sec. Last, 99.9% pure vacuum deposition grade CaF_2 was vapor deposited onto the glass substrates from a baffled source [18] at a rate of 0.2 nm/sec. The entire sample was exposed during the CaF_2 evaporation except for a 1.5-mm strip along each 4.45-cm edge where the contact pads are located. The mask used to define the exposed area during the CaF_2 evaporation was 1.6 mm thick and mounted snugly against the sample. The temperature of the sample increased with CaF_2 deposition time starting from room temperature. Following the deposition, the sample was allowed to rest in the bell jar for 10 min, removed (briefly exposed to air) and then stored under vacuum. The value of the film coverage d, used to identify each sample, was determined from the deposition observed on a quartz crystal microbalance (QCM), measured simultaneously with the deposition on each glass substrate. The coverage d is reported here as a nominal film thickness presuming the bulk density of CaF_2. Due to the nonzero porosity of the CaF_2 films the thicknesses measured by the QCM, d, are only nominal, and the samples are referred to by these nominal thicknesses. The contribution to the actual film thickness h_{Total} from the CaF_2 is d. The two quantities d and h_{Total} are related by $h_{Total}=d/(1-\phi)$ with the porosity $\phi=0.462\pm0.006$, independent of coverage (see Sec. III B). Samples in set II were created with the following nominal thicknesses, as measured by the QCM: 50, 125, 220, 370, 520 nm, and plain glass (no CaF_2).

The samples fabricated exclusively for surface structure investigations constitute set I. The substrates were uncut glass microscope slides 7.62×2.54 cm. CaF_2 was deposited on the substrates (i.e., no Ag, no Al) using the same procedure as for the substrates in set II. A 1.6-mm-thick mask covered a 1.5-mm strip along the entire perimeter of the glass slide. Samples in set I consisted of the following nominal thicknesses: 30, 50, 90, 69.5, 125, 175, 220, 270, 300, 330, 370, 450, and 520 nm. Fabrication of samples with thicknesses equal to those in set II allowed for a check of the reproducibility of the surfaces. This also provided evidence for the absence of significant surface structure modification due to the large temperature range experienced by the set II samples.

B. Experimental measurements

Under ambient conditions (air, room temperature) several images were taken of each sample using AFM. The images were taken at random locations sufficiently away from the glass-CaF_2 boundary and the narrow Al and Ag bands on the set II samples. The scan size of the set II samples was 2×2 μm. The scan size of the set I samples was 2×2 μm for $d\geqslant90$ nm and 1×1 μm for $d\leqslant125$ nm. Images of both scan sizes were taken for $d=90$ and 125 nm. The AFM scanning was done in tapping mode at a rate of 1 Hz with a silicon tip of spring constant 40 N/m. The nominal radius of the tip, as stated by the manufacturer specifications is less than 10 nm. Scanning the surfaces in tapping mode increases the lateral resolution, and we estimate our lateral resolution to be less than 5 nm. However, our ability to measure the overall morphology of the CaF_2 surface is somewhat limited due to the curvature of the AFM tip. After the first image was taken the sample was rotated approximately 90° and a second image was taken. The images showed no evidence of anisotropy.

The height of the CaF_2 film on each sample was measured using a profilometer. The profilometer consists of a stylus with a radius of 12.5 μm, that moves across the glass-CaF_2 boundary of the sample measuring the height profile. The measurements were done by placing the sample so the stylus of the profilometer started on the 1.5-mm strip not covered with CaF_2 and then moved through the CaF_2 boundary, and also in the opposite direction. A total of four measurements were taken on each substrate, each one at a different location on the perimeter of the substrate. Due to the large radius of the stylus, relative to the surface features of the CaF_2, the detailed surface structure cannot be detected using the profilometer.

III. SURFACE CHARACTERIZATION

A. AFM: Sample sets I and II

Representative images taken by AFM are shown in Fig. 1. Each image is 512×512 pixels in size, and the values of the pixels, which correspond to the height of the surface at each location, form a matrix Γ. The vertical height given by each matrix element is measured from a plane, such that the average of all elements is defined to be zero. Clearly, from these images the structure changes with increasing thickness of CaF_2. The structures become larger both in height and width, with increasing deposition thickness. The typical vertical length scale of an image is quantified by constructing a histogram, normalized to unity, of the matrix elements of Γ, and fitting the histogram data to a normal distribution. Our measure of the typical size of the vertical topography is given by the width of the best fit normal distribution σ_z. Figure 2 shows typical height distributions and best fits for various selected surfaces.

The surface height profiles of all surfaces is nearly Gaussian as is represented in Fig. 2. As a better measure of the

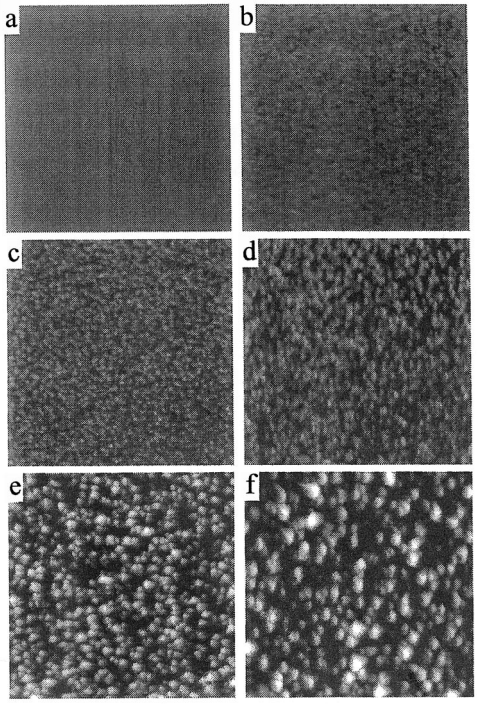

FIG. 1. Typical 2×2-μm images produced from the AFM scans of the surfaces of the following nominal thickness of CaF_2 in nm: (a) 0 (plain glass), (b) 50, (c) 125, (d) 220, (e) 370, and (f) 520. The size of the structure increases with increasing CaF_2 thickness.

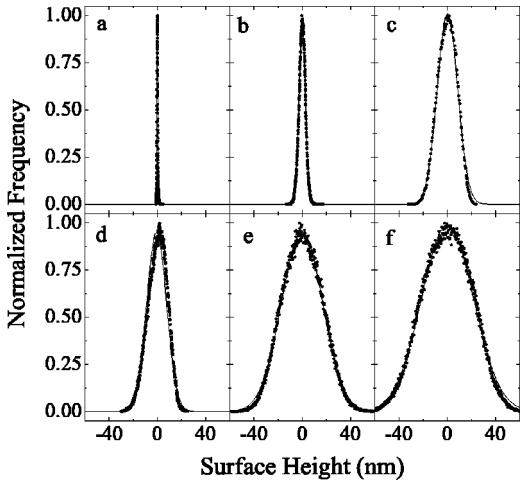

FIG. 2. Typical distributions, normalized to unity, of the heights obtained from set II AFM images of the following nominal thickness of CaF_2 in nm: (a) 0 (plain glass), (b) 50, (c) 125, (d) 220, (e) 370, and (f) 520. Solid lines indicate fits to a normal distribution of width σ_z.

Gaussian nature of the height profiles for each image we calculate the skewness m_3 and kurtosis m_4, defined as

$$m_3 = \frac{\langle [h(\vec{r},t) - \overline{h}(L,t)]^3 \rangle}{\sigma^3}, \tag{1}$$

$$m_4 = \frac{\langle [h(\vec{r},t) - \overline{h}(L,t)]^4 \rangle}{\sigma^4}, \tag{2}$$

where $\sigma^2 = \langle [h(\vec{r},t) - \overline{h}(L,t)]^2 \rangle$ is the variance of the heights. The brackets denote an average over all pixels on a single image. $h(\vec{r},t)$ is the height of the surface at $\vec{r}$ and time t and $\overline{h}(L,t)$ is the mean height of the image of size L. Since the samples were fabricated using a constant deposition rate, the time t, which is the typical parameter for relevant theoretical work, is a measure of d. In other words different times refer to samples with different film thicknesses. If the height profiles were perfectly Gaussian, then $\sigma = \sigma_z$. The skewness measures the symmetry of the profile about its mean and is zero for a true Gaussian. A positive (negative) skewness means that the points further from the mean of the distribution are more likely to be above (below) the mean surface level. The kurtosis is a measure of the peakedness of the distribution. If the distribution is relatively large near the mean and the tails of the distribution, while being relatively small at intermediate values, then the kurtosis of the distribution is larger than that of a Gaussian ($m_4 = 3$ for a Gaussian). This means that the kurtosis is sensitive to outliers. If a distribution is such that it has a larger (smaller) number of outliers than a Gaussian, then its kurtosis will be larger (smaller) than 3. Figure 3 shows m_3 and m_4 for the two sets of samples, where we ensemble averaged the values. For $d > 250$ nm the height distribution of the images appears to be consistently Gaussian, whereas for $d < 250$ nm the data are more scattered away from true Gaussian values. m_3 tends to be negative in this region, while $m_4 > 3$. This indicates that the values of $h(\vec{r},t)$ furthest from $\overline{h}(L,t)$ tend to be negative. In other words, the valleys on the surface are comparatively deeper than the hills are tall for $d < 250$ nm.

To determine a typical size of the topography parallel to the substrate we calculate the correlation between subsets of the image matrix Γ. $S(\vec{r})$ is an $m \times m$ subset of Γ beginning at $\vec{r}$, where $\vec{r}$ and $\vec{r}_1$ are two component vectors in the plane of the image. We calculate the correlation coefficient Φ between $S(\vec{r})$ and $S(\vec{r}+\vec{r}_1)$ using the standard definition [19]

$$\Phi = \frac{\sum_{i,j=1}^{m} (S(\vec{r})_{ij} - \langle S(\vec{r}) \rangle)[S(\vec{r}+\vec{r}_1)_{ij} - \langle S(\vec{r}+\vec{r}_1) \rangle]}{\sqrt{\sum_{i,j=1}^{m} [S(\vec{r})_{ij} - \langle S(\vec{r}) \rangle]^2} \sqrt{\sum_{i,j=1}^{m} [S(\vec{r}+\vec{r}_1)_{ij} - \langle S(\vec{r}+\vec{r}_1) \rangle]^2}}, \tag{3}$$

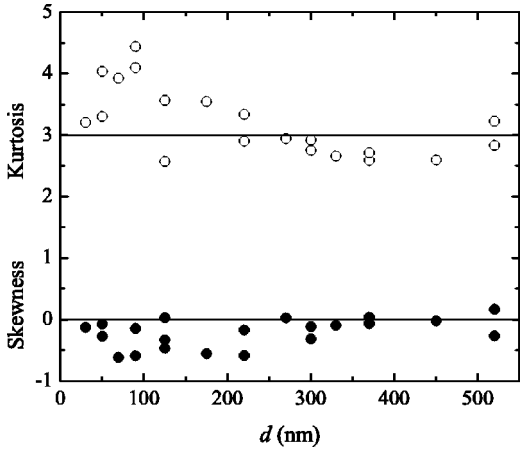

FIG. 3. Plot of skewness (filled symbols) and kurtosis (open symbols) vs d. The solid lines are the values of m_3 and m_4 for a pure Gaussian distribution.

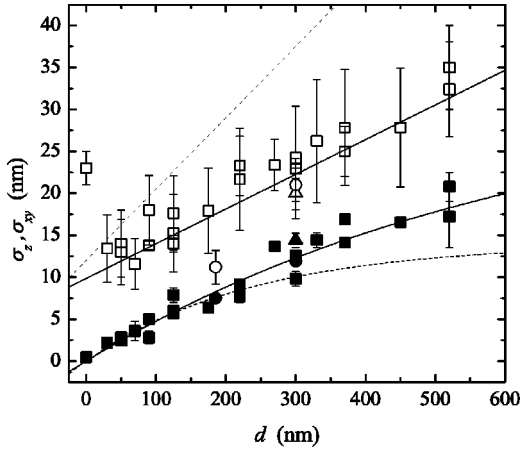

FIG. 5. Topographic length scales as measured using AFM as a function of nominal CaF_2 thickness d. Filled symbols are σ_z and open symbols are σ_{xy}. Squares denote data taken from this experiment, triangular points were taken from Ref. [16], and circular points were taken from Ref. [17]. The points corresponding to $d=0$ nm are plain glass substrates (i.e., no CaF_2). Solid lines indicate functional fits, as described in the text, and the dashed lines are the results of Varnier *et al.* [8] shown for comparison.

where the brackets denote an average over all matrix elements of S. $\vec{r}_1$ is scanned to cover all adjacent and overlapping subsets of $S(\vec{r})$, where the Φ corresponding to each $\vec{r}_1$ form the elements of the $2m+1\times 2m+1$ square matrix Λ. In other words, the element $\Lambda_{1,1}$ is the correlation between $S(\vec{r})$ and the adjacent subset in the upper left corner of $S(\vec{r})$. As $\vec{r}_1\rightarrow 0$ the subsets become increasingly overlapping and at $\vec{r}_1=0$, the subsets completely overlap so $\Phi_{\vec{r}_1=0}=\Lambda_{m+1,m+1}=1$. The element $\Lambda_{2m+1,2m+1}$ is the correlation between $S(\vec{r})$ and the adjacent subset in the lower right corner. Ideally one would like to calculate Λ for all $\vec{r}$, i.e., all subsets $S(\vec{r})$ of Γ, but due to the large computational resources necessary for such a calculation, we only calculate a Λ for 25 different values of $\vec{r}$. The results obtained using 25 values of $\vec{r}$ are in agreement with several trial calculations averaging over a greater number of $\vec{r}$, indicating that using 25 values is sufficiently representative and allows us to avoid averaging over all $\vec{r}$. To compare the horizontal length scales, we define the function

$$G(\vec{r}_1)=\langle\Lambda\rangle, \tag{4}$$

where the brackets denote the average over different values of $\vec{r}$. Figure 4 shows typical plots of $G(\vec{r}_1)$ calculated from

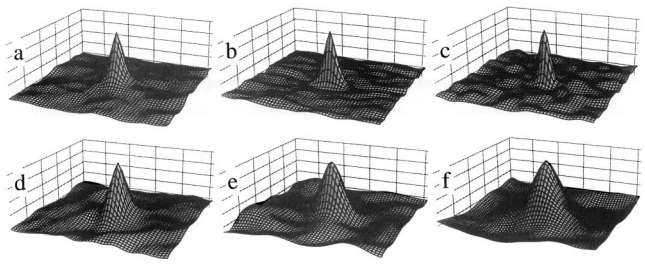

FIG. 4. (Color online) Typical plots of the function $G(\vec{r}_1)$ with $m=50$ pixels obtained from 2×2-μm set II AFM images of the following nominal thickness of CaF_2 in nm: (a) 0 (plain glass), (b) 50, (c) 125, (d) 220, (e) 370, and (f) 520. The horizontal axes are the components of the vector $\vec{r}_1$ each ranging from −50 to 50 pixels and the vertical axes show $G(\vec{r}_1)$ with the peaks normalized to unity.

2×2-μm images for various samples with $m=50$ pixels. $G(\vec{r}_1)$ is well represented by a bivariate Gaussian distribution, namely $\exp(-\vec{r}_1^2/2\sigma_{xy}^2)$, with width σ_{xy}. The width of the distribution is what we use to quantitatively compare the horizontal topography of the surfaces.

The definition of the topographic length scales that we use here differs from that of previous authors. Typically authors have defined an autocovariance function and used that to determine both the vertical and horizontal length scales of the surfaces, by fitting a Gaussian function of the form, $\delta_a^2\exp(-\vec{r}_1^2/2\sigma_{ACF}^2)$ to the autocovariance function calculated from the raw data. In their analysis, δ_a is the measure of the vertical topography and σ_{ACF} the typical horizontal topography (see, e.g., Ref. [20]). Although the definitions of the vertical length scale parameters are different, the values should be similar so that quantitative comparisons can be made [20]. The function $G(\vec{r}_1)$ is similar to the autocovariance function defined by other authors, and since the the average of all elements of Γ is zero, the only difference in the functions is the normalization. Since it is the widths of these functions that define the lengths of the horizontal topography, a direct quantitative comparison can be made between our results and those of other authors.

Figure 5 shows both σ_z and σ_{xy} as a function of nominal CaF_2 thickness d, where we have included several data points from previously published results. Overall the results from set I and set II were in agreement and therefore no distinction is made be between the two sets in this plot and many of the other plots to be presented here. The values of σ_z and σ_{xy} for $d=0$ nm are those for glass with no CaF_2. We include them in the plots to be thorough, but eschew them from the functional fits described below.

The σ_z data (filled symbols) show an increasing trend. The solid line in the figure shows a fit of the data to a function of the form $A(1-e^{-d/d_0})$, with $A=33\pm 1$ nm and d_0

$=640\pm30$ nm. This functional form incorporates the physical restriction that σ_z must be bounded as $d\rightarrow\infty$, which is consistent with our results and those of Varnier *et al.* [8], who report results for the the fitting parameters A and d_0 of 14 and 238 nm, respectively.

The results for σ_{xy} (open symbols) as a function of d are shown in Fig. 5. A fit to a straight line, omitting the plain glass value represented by $d=0$ nm, yields a slope of 0.041 ± 0.003, with a vertical axis intercept of 9.7 ± 0.7 nm. For $d<100$ nm the data are in statistical agreement with the linear fit but may show a hint of a possible flattening trend near $\sigma_{xy}=12.5$ nm. A distinction cannot be made between these possibilities due to the error of the data points. It should be noted that our resolution is limited by the the finite size of the tip used during the AFM scans (see Sec. II B). As a result the lower values of σ_{xy} may be artificially high. Varnier *et al.* have reported results with a slope of 0.085 and an intercept of the vertical axis equal to 12 nm. The intercept is outside of our range of error, but the difference is not large. The slopes, on the other hand, differ by roughly a factor of 2.

The functional fits for σ_z and σ_{xy} as a function of d as reported by Varnier *et al.* are shown as dashed lines in Fig. 5 and ours are shown as solid lines. For small values of d all results are in good agreement for σ_z and modest agreement for σ_{xy}. The largest discrepancies occur at large d where the structures reported by Varnier *et al.* are shorter and wider than the structures on our samples. Varnier *et al.* samples were fabricated using a deposition rate of 1.5 nm/sec. at a pressure of 10 μT. Their deposition rate is larger than ours by a factor of 7.5 and the pressure is twice as large as ours. These factors undoubtedly change the roughness of the deposited CaF_2, and may account for the differences. We have not carried out a detailed study of the effect of different deposition rates and pressures. Naïvely one might expect that a faster rate of deposition at higher pressure would create a rougher film. However, using a larger deposition rate would probably result in the substrate having a higher temperature during deposition when compared to a smaller rate. This higher substrate temperature might increase the surface diffusion of the deposited particles which should have a smoothing effect, leading to shorter and wider structures. Another possible explanation for the differences may be instrumental; Varnier *et al.* used a replication technique, whereas we imaged the surface directly. Our technique may be more capable of probing deeper into the surface features resulting in a wider height distribution and consequently larger values of σ_z, but this does not explain the discrepancies in σ_{xy}. An additional influence on the the measurement of σ_{xy} at small d may be the roughness of the glass substrate itself. As indicated by the $d=0$ nm points in Fig. 5, the glass substrate has very little vertical structure, $\sigma_z=0.4\pm0.2$ nm, but the structures tend to be fairly wide with $\sigma_{xy}=23\pm2$ nm. For the CaF_2 surfaces, as the film gets thicker and the structures get taller, $G(\vec{r}_1)$ will be less sensitive to the background roughness of the glass substrate. Therefore the structure of glass may influence σ_{xy} at small d but not at large d where we see significant differences. Since Varnier *et al.* did not report the uncertainty for their measurements nor did they report roughness parameters for their plain glass substrates, the discussion of the comparisons is only speculative.

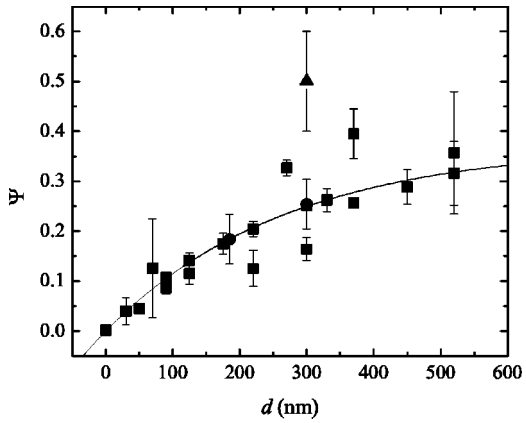

FIG. 6. The fractional increase in area Ψ vs nominal CaF_2 thickness d. Squares denote data taken from this experiment, the triangular point was taken from Ref. [16] and circular points were taken from Ref. [17]. The point corresponding to $d=0$ nm is from the plain glass substrate (i.e., no CaF_2). The solid line is a function fit to the data as described in the text.

Several other groups investigated how the roughness of CaF_2 changes with film thickness [3,4,6]. These experiments coated the CaF_2 with a layer of Ag, and used surface plasmon techniques to measure σ_z. The values of σ_z found in this manner are on the order of tenths of nanometers when d is small and several nanometers as d gets larger. The values we report are much larger than these. The difference is probably due to the overcoating of Ag deposited atop the CaF_2, as has been suggested prevoiusly [8].

The AFM measurements also allow us to estimate the increase in surface area due to the roughness. By knowing the distance between pixels and the height of each pixel contained in Γ, an effective surface area was calculated. It should be noted that this estimate does not include any surface area that is inaccessible to the AFM. The quantity Ψ used for comparison is the fractional increase of surface area from that of a flat interface. We define $\Psi=A_{AFM}/A_{flat}-1$, where A_{AFM} is the surface area calculated from the matrix Γ, and A_{flat} is the surface area of an ideally flat surface of the same size, i.e., $A_{flat}=2\times2$ μm or 1×1 μm. This definition was chosen so $\Psi=0$ for a flat surface, which facilitates our functional fit described below. Figure 6 shows Ψ as a function of d, where again we have included several previously published data points. Ψ increases as d increases. Again we have fit the data to a function of the form $A(1-e^{-d/d_0})$ resulting in $A=0.37\pm0.02$ and $d_0=270\pm20$ nm. This function satisfies the condition that the increase in area must be bounded as $d\rightarrow\infty$. The scatter in the data increases noticeably for $d\geqslant220$ nm. The point taken from Ref. [16] is the most anomalous. The general behavior of the data is in agreement with that of σ_z shown in Fig. 5, which is expected.

B. Profilometer: Sample sets I and II

Representative height profiles of the CaF_2 relative to the glass substrate are shown in Fig. 7. Immediately following the steep step in each profile there is a region with a much

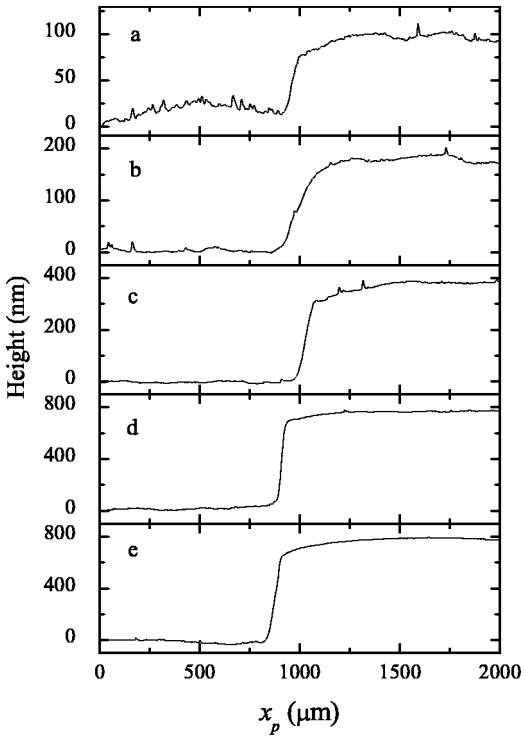

FIG. 7. Representative plots of the height profiles measured across the set II CaF_2 deposition boundary of the following nominal thickness of CaF_2 in nm: (a) 50, (b) 125, (c) 220, (d) 370, (e) 520. Note the differing scale on the vertical axis for each panel.

smaller nonzero slope that continues for a maximum of ~500 μm. This most likely originates from shadowing effects caused by the finite thickness of the mask used during deposition. The step height was defined as the difference of the baseline at small x_p and the baseline at large x_p beyond the sloped region that resulted from the shadowing effect. From the size of the steps we can calculate the the porosity of the CaF_2 film. The porosity is defined as $\phi = V_{pores}/V_{Total}$, where V_{pores} is the volume of the pores or voids in the film, and V_{Total} is the total volume of the CaF_2 and pores. V_{pores} is defined to include voids on the surface and in the bulk of film. By making the reasonable assumption that ϕ is independent of the lateral position on the CaF_2 surface and then choosing an arbitrary area, the porosity reduces to

$$\phi = 1 - \frac{d}{h_{Total}}, \tag{5}$$

where h_{Total} is the total height of the deposited film as measured by the profilometer and d is the nominal film thickness assuming bulk density as measured during deposition using a QCM. Rearranging Eq. (5), suggests that a plot of h_{Total} versus d should be linear with a slope of $(1-\phi)^{-1}$, provided ϕ is independent of d. Figure 8 shows the data for each nominal film thickness. The values of h_{Total} are averaged from four step-height measurements taken from various different locations around the perimeter of each sample. As indicated by the solid line, a linear fit to the data shows that the porosity is relatively constant over the entire range of nominal film thicknesses, with $\phi = 0.462 \pm 0.006$. We note that the uncertainty reported here is a result of scatter in the data. There may be a systematic error present due to the differences in measurement techniques of d and h_{Total}. Using thin films of Ag and Au, assumed to be largely nonporous, we estimate that results in film thicknesses can be ~10% higher from the profilometer. Such tests cannot be done using CaF_2, due to its nonzero porosity.

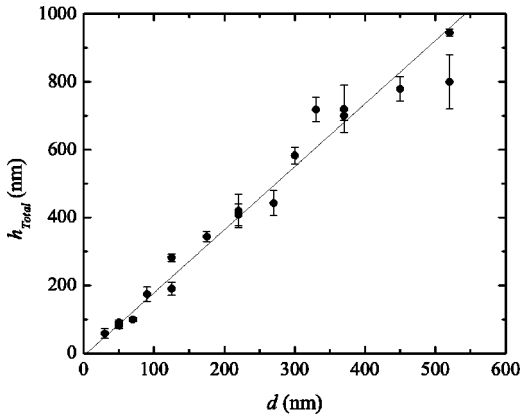

FIG. 8. Plot of h_{Total} vs d for all samples. The solid line indicates a fit to Eq. (5) resulting in $\phi = 0.462 \pm 0.006$.

At first thought a constant porosity seems logical. If a particular film thickness has a density of equal-sized pores, then as you increase the film thickness, and assuming the density and size of the pores remains the same in the added film, the porosity will remain constant. However, considering Figs. 1 and 5, as d increases, the size of the surface structure also increases, but the number of structures decrease, as is evident from Fig. 1. Assuming that the pore size can be reasonably estimated by the surface structure size, as the pore size increases and the number of pores decrease, the porosity does not change. Interestingly, this suggests that these changes produce a canceling effect, resulting in the porosity being independent of the film thickness.

C. Sample set III

A third set of substrates was fabricated using gold plated glass. These samples were glass microscope slides, similar to those used in sets I and II, cut to 1.27×2.54 cm. 50 nm of gold was thermally deposited onto all set III samples simultaneously with a deposition rate of 1.0 nm/sec. CaF_2 was then deposited over approximately half of the gold film. This was done to allow AFM imaging of the gold surface and the deposited CaF_2 as well as provide a boundary for profilometer measurements. Samples in set III were fabricated with a more limited range of nominal thicknesses equal to 10, 20, 30, 60, 90, and 120 nm. AFM was used to produce 1×1 -μm images of the surfaces and profilometer measurements were made in the same fashion as previously described.

Figure 9 shows the surface parameters (solid symbols) for the set III samples as a function of nominal CaF_2 thickness d. The data from sets I and II (open symbols) are also shown for comparison. The $d = 0$-nm points correspond to the gold film for the set III data and $d = 0$ nm corresponds to plain glass for the data from sets I and II. The skewness and kur-

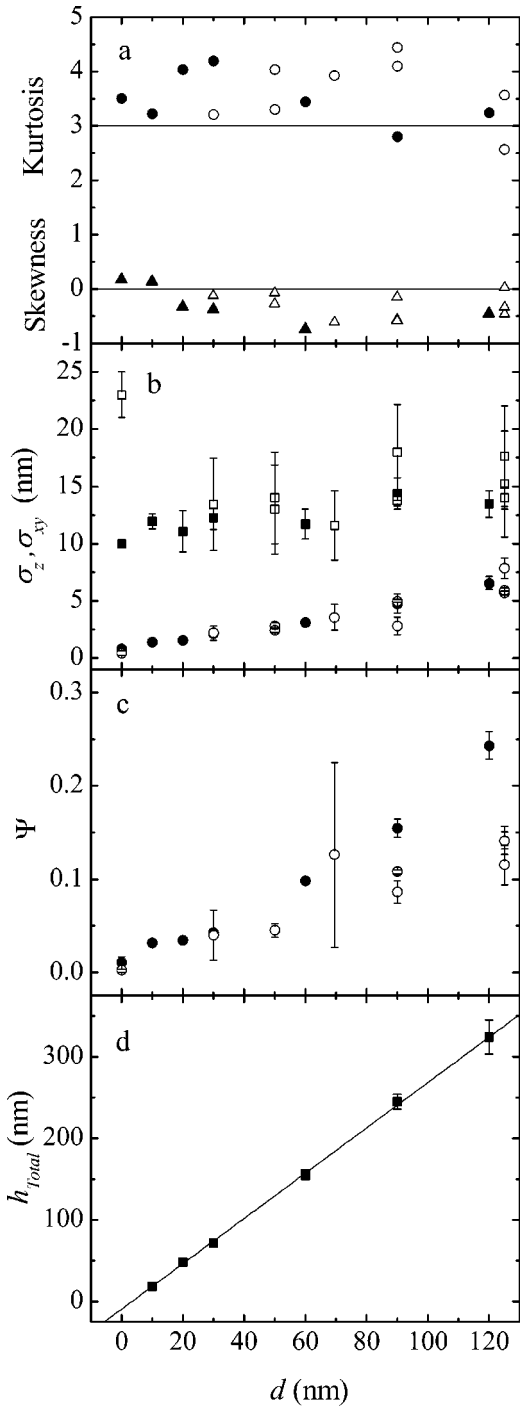

FIG. 9. Surface parameters for sample set III, CaF_2 deposited on gold (solid symbols) vs d. The data from sets I and II (open symbols) are repeated in these plots for comparison. The $d=0$ nm points correspond to gold and plain glass for set III, and sets I and II, respectively. The circles in (a) are the kurtosis and the triangles are the skewness and the solid lines are the values for a Gaussian distribution. In (b) the squares are σ_{xy} and the circles indicate σ_z. The solid line in (d) is a linear fit to Eq. (5) resulting in $\phi=0.64\pm0.01$.

tosis show very good agreement between the glass substrates and the gold-plated glass substrates, as do the values of σ_z and σ_{xy}. On the other hand, the fractional increase in area Ψ begins to disagree as d gets larger, with larger values of Ψ for the gold plated substrates. The porosity determined from a linear fit of Eq. (5) yields $\phi=0.64\pm0.01$ (see Sec. III B regarding the reported error) for the gold plate substrates which is 39% larger than the porosity found for the set I and II data. See Sec. IV D for a further discussion involving the differences between CaF_2 on glass and CaF_2 on gold plated glass.

IV. SCALING ANALYSIS

A. Background

The goal of the current section is to present a different analysis of the surface data from that of the previous section. Specifically, we will reveal the fractal nature of the surfaces and the scaling behavior. To motivate this analysis we define the interface width $w(L,t)$ of the two dimensional surface of size $L\times L$, which in our case is the image size, at time t as [12]

$$w(L,t)=\sqrt{\left\langle \frac{1}{L^2}\int d^2r[h(\vec{r},t)-\overline{h}(L,t)]^2\right\rangle}. \tag{6}$$

Here $\vec{r}$ is the vector defining the lateral position on the substrate. For a given surface, $h(\vec{r},t)$ is the height at position $\vec{r}$ and $\overline{h}(L,t)$ is defined to be the mean height. These variables are the same as defined in Sec. III. The initial condition defining the variables at $t=0$ is that of a flat interface. The brackets denote an average over different realizations, or in other words, over different locations on the same sample. Family and Vicsek [21] conjectured that rescaling space by a factor of b and time by a factor b^z rescales $w(L,t)$ by a factor of b^α ultimately implying that

$$w(L,t)\sim L^\alpha f(t/L^z), \tag{7}$$

where $f(x)$ is a scaling function. If, for a given system size L, $w(L,t)$ saturates as time gets large then $f(x)\rightarrow$ constant as $x\rightarrow\infty$. This saturation occurs when

$$t\sim L^z \tag{8}$$

and at that time the system is said to be correlated or in other words $\xi_\parallel=L$, where $\xi_\parallel$ is called the correlation length parallel to the substrate. Replacing L in Eq. (8) with $\xi_\parallel$, which in fact also holds for times less than the saturation time, we get

$$\xi_\parallel\sim t^{1/z}. \tag{9}$$

This then implies [21] that before saturation $w(L,t)$ must be independent of L with

$$f(x)\sim x^\beta \quad \text{and} \quad \beta=\alpha/z \tag{10}$$

and thus

$$w(L,t)\sim t^\beta, \quad 1\ll t\ll L^z \tag{11}$$

and when the time is larger than the saturation time, i.e., $t\gg L^z$, the width is sensitive to the system size as $w(L,t)\sim L^\alpha$. The roughness exponent α characterizes the self-affinity of the surface and the dynamic exponent z characterizes the dynamics.

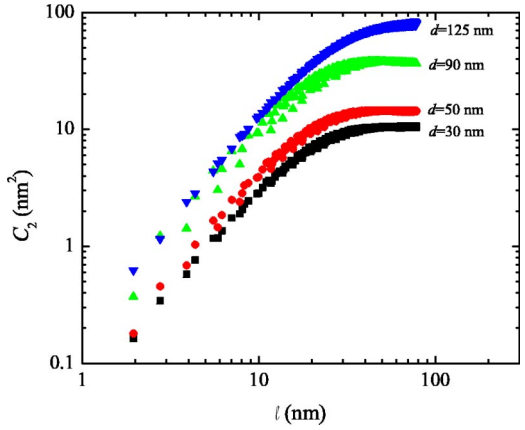

FIG. 10. (Color online) $C_2(\ell)$ vs ℓ for several of the 1×1-μm sets of images.

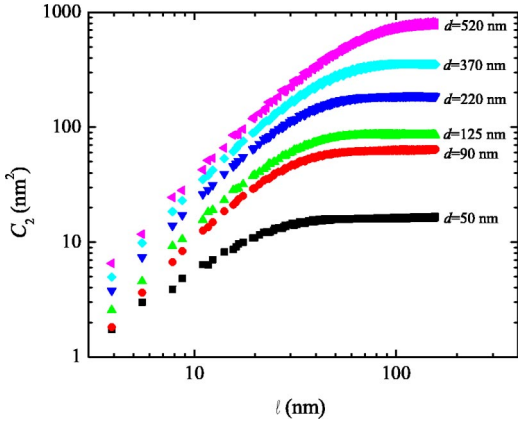

FIG. 11. (Color online) $C_2(\ell)$ vs ℓ for several of the 2×2-μm sets of images.

The task then becomes to determine the values of these finite size scaling exponents. Theoretically this can be done for a particular model using its stochastic growth equation, either analytically or numerically. Various models have been solved in this way in $1+1$ dimensions and to a lesser extent in $2+1$ dimensions. The set of critical exponents for a particular model determines the universality class of the model. The above treatment is applicable to the growth of a variety of interfaces, such as fluid flow in a porous medium, the propagation of burning fronts, biological growth, etc. [10]. Another experimental realization of interface growth is thin film deposition, which occurs in $2+1$dimensions. An assortment of systems have already been investigated, including for example, the vapor deposition of V_2O_5 [22] on Si, Si on Si [23], Au on glass [24], and in a number of other experiments some of which use ion bombardment and sputter deposition (see, e.g., Ref. [10]).

Measurement of the saturation values of $w(L,t)$ for different system sizes is usually not a practical way to experimentally determine α due to the large saturation times for macroscopic surfaces. Therefore to determine α for our system of CaF_2 on glass, we first calculate the height-height correlation functions of the surface, as is commonly done [25]. For our system, we define the qth order height-height correlation function as

$$C_q(\ell) = \left\langle \left\langle \frac{1}{L^2} \int d^2r |h(\vec{r},t) - h(\vec{r}+\vec{\ell},t)|^q \right\rangle \right\rangle_{|\vec{\ell}|=\ell}, \quad (12)$$

where the inner brackets denote an ensemble average and the outer brackets denote a radial average. The radial average reduces the dependence of $C_q(\ell)$ to the distance ℓ between two points and ignores the particular orientation of the two points. All ensemble averages in this report are over two realizations of the system. Although not immediately obvious, if $\ell < \xi_{\|}$ then $C_q(\ell)$ scales as [25]

$$C_q(\ell) \sim \ell^{\gamma_q} \quad (13)$$

and $\alpha = \gamma_2/2$ [10]. To determine β we can measure $w(L,t)$ vs t, as indicated by Eq. (11) . The value of β can also be determined from $C_2(\ell)$ [10], if $t \ll L^z$ then as $\ell \to \infty$,

$$C_2(\infty) \sim t^{2\beta}. \quad (14)$$

As previously mentioned, depositing the CaF_2 at a constant rate provides for a simple relation between nominal film thickness and time, namely $t \sim d$.

B. Results

Figures 10 and 11 show typical log-log plots of $C_2(\ell)$ as a function of ℓ for various values of d. To reduce computation time $C_2(\ell)$ was calculated only for $\ell \leqslant \ell_{max}$ where $\ell_{max}=40$ pixels for both images sizes, therefore $\ell_{max}=156$ nm for the 2×2-μm images and $\ell_{max}=78$ nm for the 1×1-μm images. We fit $C_2(\ell)$ vs ℓ to a function of the form $A_2\ell^{\gamma_2}$ for small ℓ, which gives us $\alpha=\gamma_2/2$ for each value of d. Since the resulting values of γ_2 differ slightly for each value of d, as discussed below, we have scaled the prefactors A_2 by d^{γ_2} so that all data points have identical units. $A_2d^{\gamma_2}$ vs d is shown in Fig. 12 on a log-log scale. We have fit the data to a power law, excluding the $d=50$ and 520-nm points from set II, which produced anomalous values of α (see below). The result is shown by the solid which has the functional form ad^b, where $a=0.004\pm0.001$ and $b=2.59\pm0.07$.

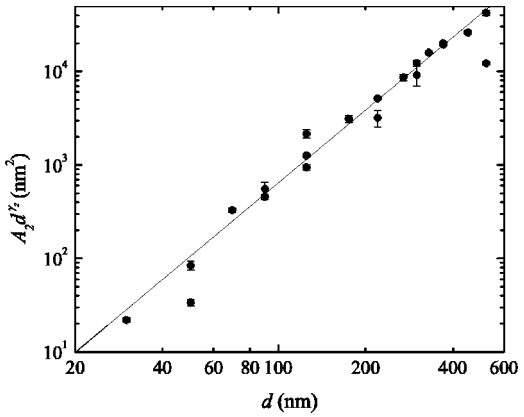

FIG. 12. $A_2d^{\gamma_2}$ vs d on log-log scales. The solid is a power-law fit to the data, ad^b, where $a=0.004\pm0.001$ and $b=2.59\pm0.07$. See the text for further discussion.

TABLE I. Values of α deduced from linear fits to the second height-height correlation function $C_2(\ell)$ for small ℓ. The values of α found by including n_f-4 and n_f+4 points in the linear fit are also shown. The reported error is the statistical error calculated from the linear fit for α. See the text for further discussion on the error of α.

Set	$L(\mu\text{m})$	d(nm)	n_f	α	Error	α_{n_f-4}	α_{n_f+4}
I	1	30	12	0.88	±0.02	0.91	0.87
I	1	50	15	0.92	±0.03	0.95	0.90
II	2	50	12	0.57	±0.02	0.59	0.55
I	1	69.5	17	0.87	±0.01	0.89	0.85
I	1	90	20	0.91	±0.04	0.95	0.89
I	2	90	12	0.87	±0.01	0.90	0.84
I	1	125	21	0.91	±0.01	0.91	0.84
I	2	125	12	0.85	±0.02	0.87	0.82
II	2	125	8	0.88	±0.03	0.93	0.84
I	2	175	12	0.84	±0.02	0.86	0.81
I	2	220	12	0.89	±0.01	0.91	0.86
II	2	220	15	0.88	±0.04	0.91	0.85
I	2	270	14	0.83	±0.02	0.86	0.81
I	2	300	12	0.90	±0.01	0.91	0.88
I	2	300	15	0.90	±0.04	0.93	0.87
I	2	330	13	0.90	±0.01	0.92	0.89
I	2	370	12	0.90	±0.01	0.92	0.88
II	2	370	14	0.85	±0.01	0.87	0.84
I	2	450	16	0.88	±0.01	0.90	0.87
I	2	520	16	0.89	±0.01	0.91	0.89
II	2	520	20	0.77	±0.01	0.78	0.76

The measured values of α for all sets of data are presented in Table I and plotted in Fig. 13. The majority of the data are scattered around a constant value of $\overline{\alpha}=0.88\pm0.03$, as depicted by the solid line in the figure. Two values of α were anomalously low and were not taken into account in $\overline{\alpha}$; the error for $\overline{\alpha}$ was calculated from the scatter in the data. These low values were both from set II and correspond to d

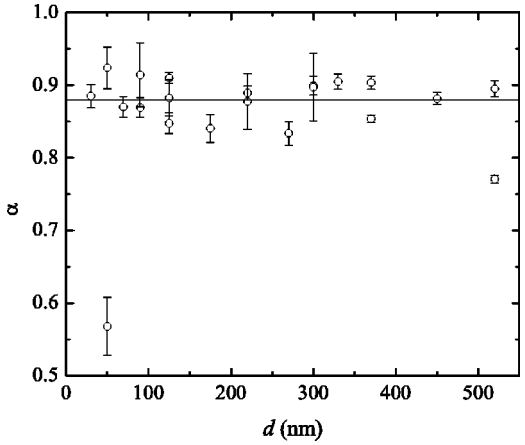

FIG. 13. α vs d for all surfaces. The solid line indicates the average value, $\overline{\alpha}=0.88\pm0.03$, excluding the two anomalously low values.

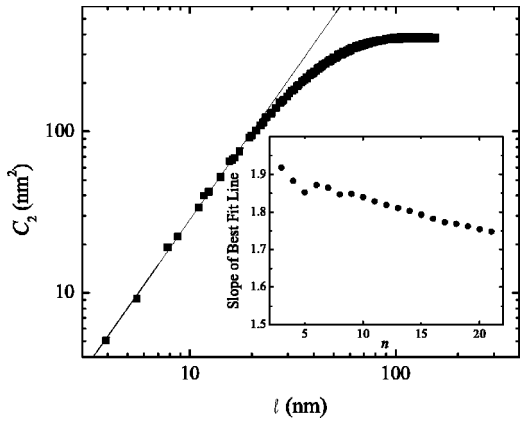

FIG. 14. $C_2(\ell)$ vs ℓ for $d=330$ nm. The solid line is the best power-law fit for small ℓ. The inset shows the slope of the best fit line on a log-log scale versus the number of points included in the fit starting from the data point corresponding to the smallest ℓ. The downward trend indicates a slight curvature in the data.

$=50$ nm and $d=520$ nm. The error bars in Fig. 13 were calculated from the fit in the usual manner [26]. It should be pointed out that most of the data used to determine α were not strictly linear, but had a very slight curvature, which may be associated with sampling effects [27]. This nearly linear behavior is illustrated in Fig. 14. Figure 14 shows $C_2(\ell)$ vs ℓ for $d=330$ nm with the solid line indicating the best power-law fit, which determines α. The data *appear* to show good linearity for $\ell\leqslant19.5$ nm which corresponds to the first 13 data points on the plot, but closer examination reveals a pseudolinear trend. The inset in Fig. 14 is a plot of the slope of the best fit line versus the number of data points n included in the fit. n is defined as starting from the first point, i.e., the point with lowest value of ℓ, for the data in Fig. 14. In other words, $n=3$ for a fit to the first three points in Fig. 14, $n=4$ for a fit to the first four points in Fig. 14, etc. The inset plot shows a subtle downward trend indicating that $C_2(\ell)$ has slight curvature, which is not readily apparent upon first inspection of the data. Due to this pseudolinear trend, the number of points that should be included in the fit to determine α is not clearly defined. The number of points included in the each fit, n_f, that yielded the reported values of α were determined visually from plots similar to Fig. 14 for each substrate. n_f was chosen to be the point beyond which the data visually deviated from the apparent linear behavior. Due to the ambiguity of this choice we have also reported the values of α determined using n_f-4 and n_f+4 for quantitative comparison. These values are included in Table I as α_{n_f-4} and α_{n_f+4}, respectively. These values either lie within the range of reported error or slightly beyond this range. This provides an indication that our values of α reported in Fig. 13 are robust.

Figure 15 shows a plot of $w(L,t)$ vs d for all sets of images. The solid line is a fit to Eq. (11) resulting in $\beta=0.75\pm0.03$ with a multiplicative prefactor of 0.17 ± 0.03. The data show good agreement with a power law over the range of studied thicknesses. We have also plotted $C_2(\infty)$ vs d in Fig. 16 where the values of $C_2(\infty)$ were determined from the plateau regions in $C_2(\ell)$ (see Figs. 10 and 11.) The solid line is a fit to Eq. (14) resulting in $\beta=0.75\pm0.03$, which is

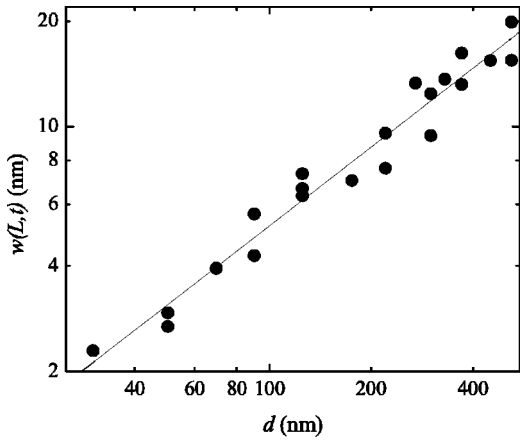

FIG. 15. Plot of $w(L,t)$ vs d (i.e., time) on a log-log scale for all sets of images. The solid line is a functional fit to a power law resulting in $\beta=0.75\pm0.03$.

identical to the value obtained from Fig. 15. The prefactor resulting from this fit is 0.05 ± 0.02. Not surprisingly, the data indicate that the interfaces have yet to reach saturation. Equation (13) only holds for $\ell<\xi_{\|}$, hence we can estimate the correlation length, $\xi_{\|}$, from the location of the plateau regions in the plots of $C_2(\ell)$. From this we estimate that $\xi_{\|}<100$ nm for all surfaces studied here. This is much less than our system size, therefore Figs. 15 and 16 should not show saturation. Using $\overline{\alpha}$ and the restriction in Eq. (10) , we can estimate $z=\alpha/\beta=1.17\pm0.06$.

Collectively the scaling behavior presented here provides evidence that the morphology of our surfaces is fractal in nature and follows the dynamical scaling description outlined in Eqs. (7)–(11). As discussed in Refs. [23,28], a distinguishing feature between a surface with a fractal-like interface and a surface consisting of a collection of fairly regular three-dimensional mounds is the existence of log-periodic fluctuations in $C_2(\ell)$ for $\ell>\xi_{\|}$ for the surface with the moundlike structures. No such fluctuations are seen in $C_2(\ell)$ for $\ell>\xi_{\|}$ (see Figs. 10, 11, and 14). This provides additional evidence for the fractal nature of our surfaces.

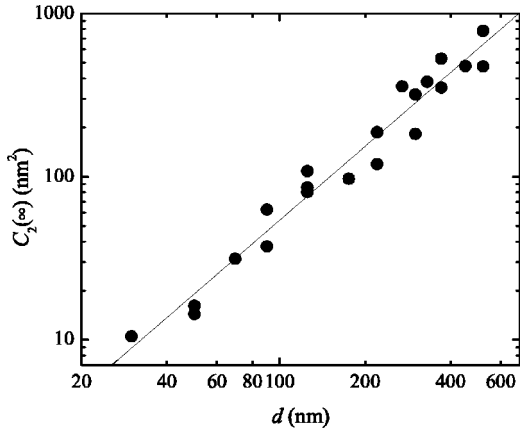

FIG. 16. Plot of $C_2(\infty)$ vs d (i.e., time) on a log-log scale for all sets of images. The solid line is a functional fit to Eq. (14) of slope 2β resulting in $\beta=0.75\pm0.03$.

C. Discussion

Much of the theoretical work done to describe the kinetic roughening process has arisen from the Kardar-Parisi-Zhang (KPZ) equation [29],

$$\frac{\partial h}{\partial t}=\nu\nabla^2 h+\frac{\lambda}{2}(\nabla h)^2+\eta. \tag{15}$$

ν is an effective surface tension and λ describes the strength of lateral growth. The roughening is introduced by the noise term η which is usually assumed to be Gaussian with

$$\langle\eta(\vec{r},t)\rangle=0 \tag{16}$$

and

$$\langle\eta(\vec{r},t)\,\eta(\vec{r}',t')\rangle\sim\delta(\vec{r}-\vec{r}')\,\delta(t-t'). \tag{17}$$

The critical exponents of Eq. (15) can be found analytically in $1+1$ dimensions ($\alpha=1/2,\beta=1/3$) and estimated numerically in $2+1$ dimensions ($\alpha=0.38,\beta=0.24$) [10]. An additional restriction due to Galilean invariance is placed on the exponents in all dimensions resulting from Eq. (15) [30–32],

$$\alpha+\frac{\alpha}{\beta}=2. \tag{18}$$

Many experimental investigations resulted in values of $\alpha>1/2$, which led to the exploration of quenched noise [10]. Zhang also proposed that a system dominated by noise that follows a power-law distribution rather than being Gaussian may lead to different exponents [33,34]. With an uncorrelated power-law probability distribution of the form

$$P(\eta)\sim\pi\begin{cases}\eta^{-(\mu+1)} & \text{for } \eta>1\\ 0 & \text{otherwise}\end{cases} \tag{19}$$

the scaling exponents of the KPZ equation were reported for a $D+1$ dimensional system to be [34,35]

$$\alpha=\frac{D+2}{\mu+1}, \tag{20}$$

$$\beta=\frac{D+2}{2\mu-D}. \tag{21}$$

Later work provided theoretical evidence that in fact these equations were exact [36,37]. Equations (20) and (21) satisfy Eq. (18) independent of μ. Equation (19) increases the probability of large noise events occurring when compared to a normal distribution where the probability decreases exponentially. These equations are likely to be valid for $D+1<\mu<\mu_c$, where there is a crossover to Gaussian-type behavior at μ_c. Several numerical simulations in $1+1$ dimensions have confirmed Eqs. (20) and (21) (see, e.g., Ref. [38]). Experimental evidence in $1+1$ dimensions for a power-law noise distribution has been provided in systems including two-phase fluid flow [39] and slow paper combustion [40,41] by measuring the noise probability distribution directly along with one or several critical exponents. In $2+1$ dimensions it appears that only one numerical simulation of the KPZ equation using Eq. (19) has confirmed the result for β in Eq. (21)

[42], and no direct experimental evidence has been presented.

In addition it has been shown numerically that uncorrelated noise with power-law-distributed amplitudes may lead to multifractality [43]. The multifractal nature is exposed by examining the scaling behavior of the qth order height-height correlation functions of the surface with [see Eqs. (12) and (13)]

$$\gamma_q = qH_q, \tag{22}$$

where H_q changes with q. For systems without multifractality, H_q is constant for all q and equals the roughening exponent α. Many authors have reported multifractality in $2+1$ dimensions for a variety of surfaces by measuring the H_q spectrum, including those that have been vacuum deposited as was done here. Although there are exceptions, most of these authors do not measure β, as they are interested in surface characterization and not in the dynamics. As a result, the question of the cause of the multifractality is often neglected. We also point out that other authors [37] suggested that $C_q(\ell)$ may not have been a well defined quantity as used for the proof of multifractality in Ref. [43]. They argued that due to the particular model used in Ref. [43], the probability distribution describing the nearest neighbor height difference δ follows a power law for large δ resulting in $C_q(\ell)$ not being a well defined quantity for large q, because $C_q(\ell)$ diverges with system size. Explicitly stated, $C_q(\ell) \to \infty$ for large q as $L \to \infty$ if

$$P(\delta) \sim \frac{1}{\delta^{\mu}} \tag{23}$$

for large δ [44]. Barabási *et al.* [43] justified the use of $C_q(\ell)$ by noting that for finite systems and a finite number of samples $C_q(\ell)$ is always meaningful. In fact it was this crossover to divergent behavior in the limit of infinite system size where the change in H_q was seen for this finite system. The change or step in H_q was dubbed a phase transition in the spectrum of H_q. In this work we interpret changing H_q as evidence for mulitfractility, due to our finite system size, and also point out evidence for Eq. (23).

In an effort to interpret our data along these lines we have plotted $C_q^{1/q}$ vs ℓ for a representative set of d in Fig. 17. For clarity only $q=1-5$, 8, 11, and 20 are plotted. When the height-height correlation functions are plotted in this way the slope of the linear region is H_q. As can be seen in the figure, H_q decreases as q increases. This is shown more explicitly in Figs. 18 and 19, which are plots of H_q as a function of q for $d \leqslant 220$ nm and $d > 220$ nm, respectively. The data are shown in two separate figures for clarity. The general trend is that for small q, $H_q \approx 0.9$ and then as q increases, H_q decreases and then approaches a constant value. These shifts in H_q as a function of q are evidence for multifractal behavior. A general trend in H_q as d changes is not apparent although for values of d greater than $d \sim 220$ nm the decrease in H_q tends to be sharper and approaches a constant value at lower H_q than for lesser values of d. Again the results from the sample with $d=50$ nm, and to a lesser extent with $d=520$ nm, both from set II are not consistent with the rest of the results. Numerical studies [45] have investigated the dependance of H_q on q for a range of values of μ, but these the simulations were performed in $1+1$ dimensions and are not generally applicable to our results.

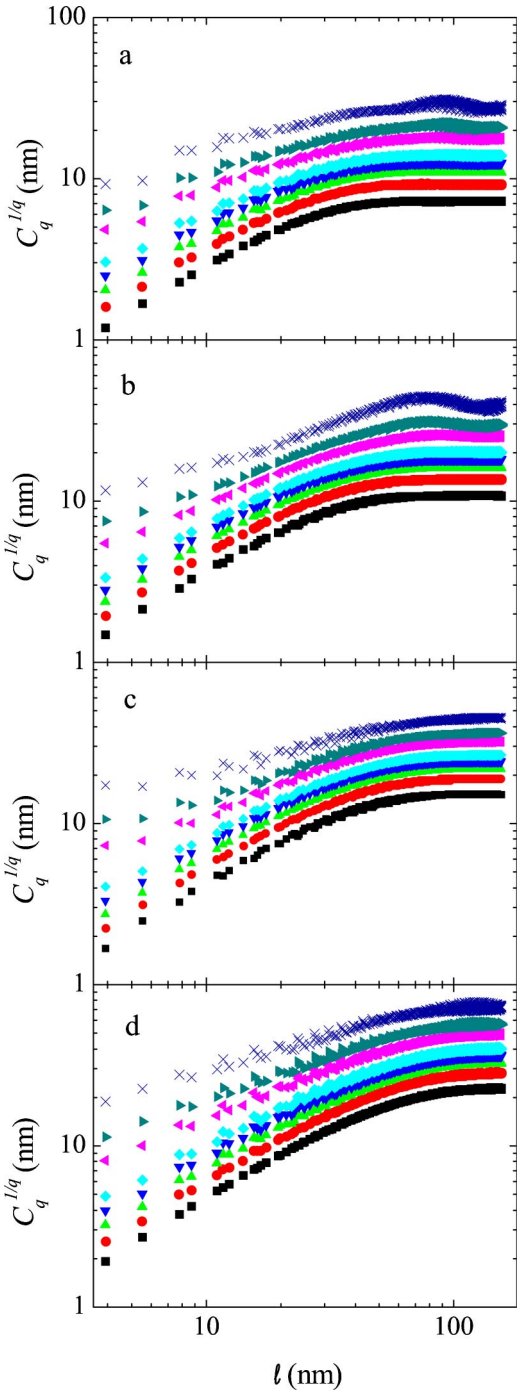

FIG. 17. (Color online) Log-log plot of $C_q^{1/q}$ vs ℓ for d equal to (a) 125 nm, (b) 220 nm, (c) 370 nm, and (d) 520 nm for different q. For clarity, C_q is shown only for select q even though $C_q^{1/q}$ was calculated for $q=1-20$. In each panel starting from the bottom and going up, $q=1$, 2, 3, 4, 5, 8, 11, and 20. H_q is the slope of each curve in the region of small ℓ, and decreases as q increases.

As mentioned, Barabási *et al.* [43] have suggested that the step in the H_q spectrum corresponds to a phase transition

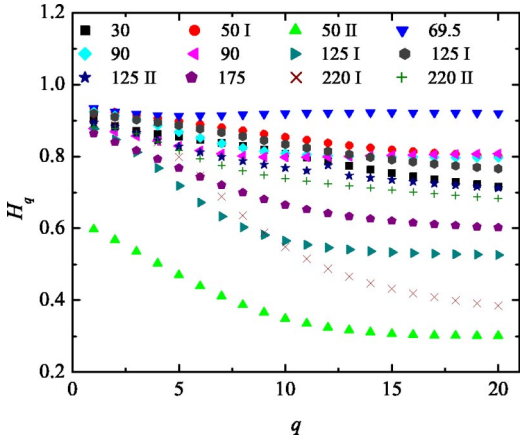

FIG. 18. (Color online) H_q vs q for $d \leqslant 220$ nm. The numbers in the legend refer to the nominal thickness of the film d in nanometers. The labels I and II refer to set I and set II, respectively, where needed.

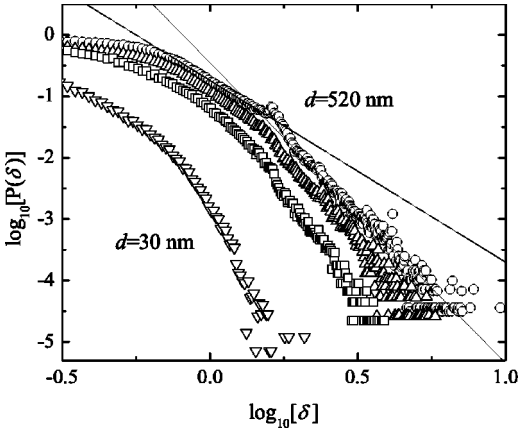

FIG. 20. $\log_{10}[P(\delta)]$ vs $\log_{10}[\delta]$ for $d=30$, 175, 300, and 520 nm corresponding to the inverted triangles, squares, triangles, and circles, respectively. There are two visible linear regions for $d \geqslant 175$ nm and only one for $d<175$ nm. The solid lines show linear fits for each linear region for $d=520$ nm.

beginning at $q=\mu$. In our case the beginning of the transition is not well defined, but a broad estimate sets the transition in the range of $q=2.5-5.0$, which implies $\mu=2.5-5.0$. We can also use our measured values of α and β to obtain a value of μ using Eqs. (20) and (21) for $D=2$. Using $\overline{\alpha}=0.88\pm0.03$ yields $\mu=3.5\pm0.2$, while using $\beta=0.75\pm0.03$ yields $\mu=3.7\pm0.1$; both values of μ are in statistical agreement and fall into the middle of the range of μ estimated from the H_q spectra. We also note for our measured values that $\alpha+\alpha/\beta=2.05\pm0.07$, which is consistent with the prediction of Eq. (18) . These results suggest the presence of power-law-distributed noise in our samples of vacuum deposited CaF_2 on glass.

Motivated by these results we then searched for the behavior indicated in Eq. (23) . We define the nearest neighbor height difference δ as

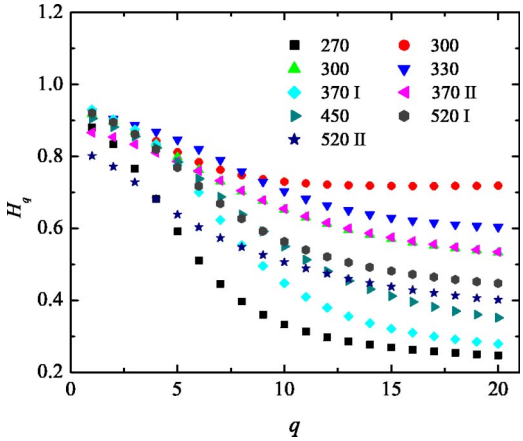

FIG. 19. (Color online) H_q vs q for $d>220$ nm. The numbers in the legend refer to the nominal thickness of the film d in nanometers. The labels I and II refer to sets I and set II, respectively, where needed.

$$\delta = \frac{|h(\vec{r},t) - h(\vec{r}+\vec{r}_{nn},t)|}{|\vec{r}_{nn}|}, \tag{24}$$

where $\vec{r}_{nn}$ is the vector pointing from $\vec{r}$ to the nearest neighbor. In our case $|\vec{r}_{nn}|=1$ pixel. δ was calculated for every nearest neighbor pair on a particular image of the surfaces. A histogram of the data, with the peak normalized to unity, provides the probability distribution $P(\delta)$. The values of $P(\delta)$ used here are averaged over several images. Figure 20 shows $\log_{10}[P(\delta)]$ plotted versus $\log_{10}[\delta]$ for $d=30$, 175, 300, and 520 nm. Mindful that the span of δ values is relatively narrow, there are two regions that show behavior consistent with a power law in samples with large d, and one region consistent with power-law behavior for samples with smaller d. Both regions occur at large δ. The solid lines in the figure indicate a linear fit for the two regions for $d=520$ nm. The first region spans roughly $\delta=0.75-1.5$ and for $\delta>1.5$ there is a crossover to a second regime that is roughly linear with a more negative exponent. As d gets smaller the first linear region shrinks until it is barely visible at $d=175$ nm, and not visible for $d<175$ nm. The second linear region is still visible for all values of d. The slope of the second linear region ranges from roughly -10 to -5 for $d=30-520$ nm. The crossover to the second linear regime is most likely indicative of a truncation in the spectrum of the noise distribution due to the finite nature of the experiments. The values of the slope in the first region are modestly close to $\mu=3.5-3.7$ obtained from α and β and are most likely related to Eq. (23). Defining those slopes as μ, Fig. 21 shows μ so determined vs d for the distributions where this linear region is visible. The solid line indicates the value of $\mu \approx 3.6$ obtained from α and β. The range of the values of μ obtained from Fig. 20 is roughly 3–5, similar to that which was estimated from Figs. 18 and 19. As stated earlier, these two features are theoretically linked and the overlapping ranges should be expected.

At small d, μ from $P(\delta)$ tends to be higher than μ from α and β and at $d \sim 250$ nm there is a crossover to lower values

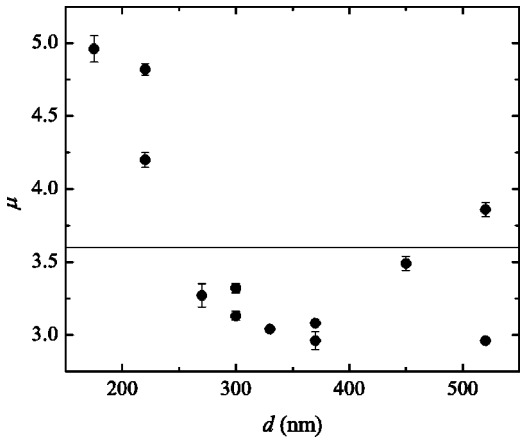

FIG. 21. μ vs d for those samples with two linear regions in $P(\delta)$. The solid line indicates μ obtained from α and β, and the error bars are taken from the linear fit.

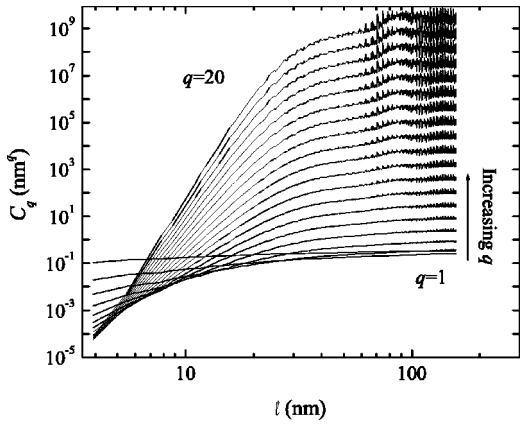

FIG. 22. $C_q(\ell)$ vs ℓ for a glass surface for $q=1-20$ on a log-log scale. The arrow indicates the direction of increasing q.

of μ. This behavior is somewhat reminiscent of the kurtosis of the height distributions plotted in Fig. 3. Earlier we argued that the high kurtosis was likely due to deep valleys on the deposited surface, as indicated by the negative skewness in that region of d. Since δ is essentially the local slope on the interface, and μ in Fig. 21 is the negative of the exponent in the power-law distribution of δ, a higher μ in Eq. (23) means that regions of large local slope are less likely. It is possible that the similar trends in these plots is coincidental, but this may also indicate that the deep valleys present on the small d samples are less likely to descend quickly when compared to the structures on the larger d samples.

Unfortunately, we are not able to measure the noise spectrum directly for further verification of a power-law distribution, but we consider our results as presented as evidence toward this type of distribution. The previously mentioned experiments in $1+1$ dimensions were able to measure the morphology of the interface directly as it grew, which allowed definition and measurement of the noise in the system [39–41]. In our system we do not directly measure a single interface as it grows, but rather grow an interface for a time t and then terminate its growth and repeat the process for a different time on a new substrate. The result is our sets of samples, which are many realizations of the noise spectrum. The fact that the results of many realizations of the noise, with the exception of two, conspire to give a single value of μ is remarkable. Collectively, the self-consistent evidence presented here allows us to conclude that our system is consistent with domination by rare noise events. This in turn suggests that our system is described by the KPZ equation dominated by power-law-distributed noise. We should point out that other models have been proposed to account for large values of α and β, which are experimentally inaccessible to us. Most notable of these is a correlated noise model, where there are spatial and/or temporal correlations in the noise spectrum [32]. The Galilean invariance that leads to Eq. (18) breaks down in the presence of temporally correlated noise, but remains valid for spatially correlated noise [32]. Since our measured values of α and β are in agreement with Eq. (18), we do not expect the presence of temporally correlated noise, nor are we aware of any physical mechanisms in our system that would lead to either spatial or temporal correlations in our noise spectrum.

Part of the difficulty in measuring the noise in our system is the lack of knowledge pertaining to the physical source of the noise. The absence of physical justification for the inclusion of power-law-distributed noise into any system has hindered the verification of this hypothesis [11,33]. Although it has been shown that power-law noise can arise in models having quenched disorder [46], such as that in the two phase fluid experiments [39,47].

Perhaps, a reasonable thought may be that our noise distribution describes the size of the grains deposited on the surface. It is possible that as the CaF_2 molecules are evaporated and moving in the vapor inside the bell jar they occasionally interact. If the energy of the molecules is low enough there is a probability that they will stick together. A rough estimate indicates that the mean free path of the CaF_2 traveling in the bell jar during evaporation is ~ 10 m compared to the distance between the deposition source and the sample which is ~ 0.4 m. Considering this, it seems unlikely that a large number multiple molecule clusters will be deposited on the surface. In the case that such an event would occur, the size of the cluster would be small and likely only contain several molecules. Consequently, it does not seem probable that our noise distribution describes the size of grains deposited on the surface.

D. Initial conditions

We have also done preliminary experiments regarding the effects of the initial growth condition on the resulting surface characteristics. Theoretical work using a Huygens principle construction to model the columnar growth of an amorphous film has indicated that the initial conditions of a sputter deposited interface can noticeably alter the morphology of the growing surface [48]. An AFM image of a glass substrate, similar to those used here, reveals very small surface structure with $w(L,0)=0.4$ nm. We did, however, see two regions of power-law scaling in $C_q(\ell)$ as shown Fig. 22. The two regions of scaling, which obey Eq. (13) , appear with a crossover at $\ell_* \approx 20$ nm for $C_1(\ell)$, which gradually increases to $\ell_* \approx 30$ nm for $C_{20}(\ell)$. Figure 23 is plot of $C_2(\ell)$ vs ℓ for

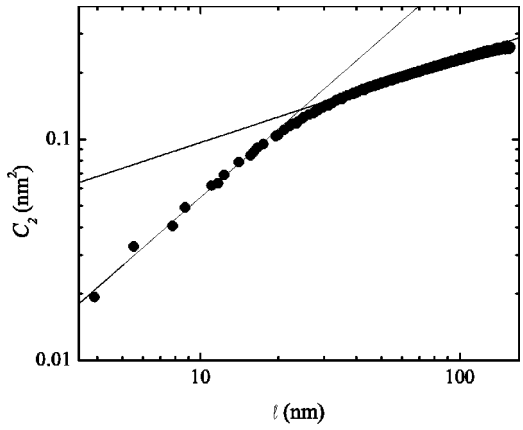

FIG. 23. $C_2(\ell)$ vs ℓ for a glass surface for on a log-log scale. The solid lines are best fits to the two linear regions, which result in $\alpha=0.51\pm0.03$ for $\ell<\ell_*$ and $\alpha=0.19\pm0.03$ for $\ell>\ell_*$.

glass, where the solid lines are functional fits to the two regions of scaling and the slopes of the lines equal 2α for each region. The roughness exponents were measured as $\alpha=0.51\pm0.03$ and $\alpha=0.19\pm0.03$ for $\ell<\ell_*$ and $\ell>\ell_*$, respectively, very different than $\overline{\alpha}=0.88$ found from CaF_2. Figure 24 shows H_q vs q for the two regions. For $\ell<\ell_*$, H_q increases and then starts to decrease at $q=9$. The step in H_q for $\ell>\ell_*$, on the other hand, is smaller in magnitude and decreases until $q=9$, at which point it becomes relatively constant with $H_q=0.1$. The regions of steepest slope in H_q for glass coincide with the values of μ determined from α and β and the steps in Figs. 18 and 19, but the values of α are significantly different, which suggests that roughness of the CaF_2 is not a direct extension of the glass roughness. The structures on the glass surface are very small in height, with $w(L,0)=0.4$ nm, but tend to be fairly wide with $\ell_*\sim20$ nm, which is also consistent with the $d=0$ nm value of σ_{xy} shown in Fig. 5. Due to the very small height fluctuations on the surface of the glass and the disagreement among the values of α, we speculate that the initial conditions of the glass substrates do not play a significant role in the growth of the structure morphology of our CaF_2 surfaces.

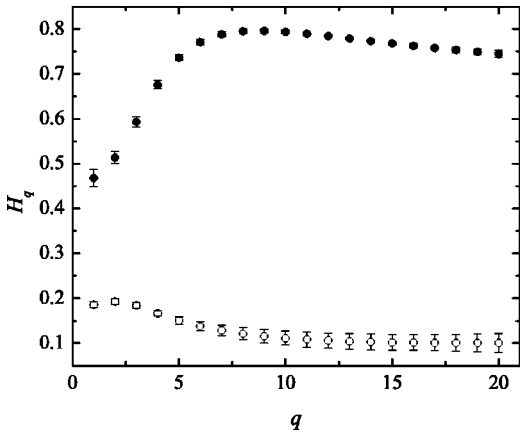

FIG. 24. H_q vs q for a glass surface. The filled symbols represent $\ell<\ell_*$ and the open symbols represent $\ell>\ell_*$. The error bars were taken from the uncertainties calculated from the best fits.

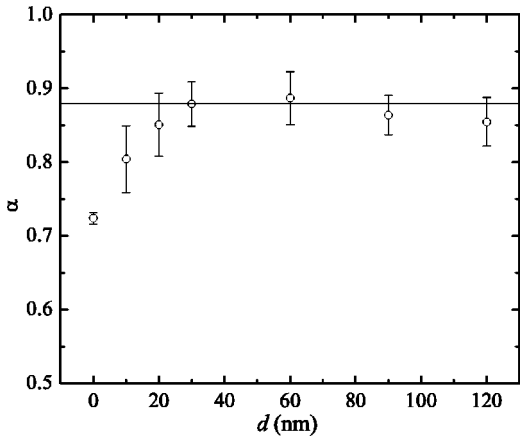

FIG. 25. α vs d for the CaF_2 on gold-plated glass samples (set III) where the $d=0$ point corresponds to the gold film. The solid line is $\overline{\alpha}=0.88$ calculated from CaF_2 on glass data.

As a further test regarding the effect of the initial conditions on the observed roughness of growing CaF_2 we can look at the data for the set III samples. The gold film surface structures are taller than those on glass with $w(L,0)=0.76$ nm and half as wide with a typical lateral length scale of ~10 nm (see Fig. 9). Figure 25 shows the values of α for the set III samples. The $d=0$-nm point represents the gold film and the solid line is the average value $\overline{\alpha}$ found for the set I and II samples of CaF_2 on glass. The data show an interesting trend for small values of d. As d increases from zero, α also increases toward the value found for the CaF_2 on glass samples and then becomes reasonably constant around $\overline{\alpha}$. Again we have scaled the prefactors by d^{γ_2} as shown in Fig. 26. The solid line in the figure is a power-law fit to the data points with $d\geqslant30$ nm resulting in ad^b, where in this case, $a=0.0007\pm0.0001$ and $b=2.21\pm0.06$. The values from this fit are not in statistical agreement with values found for CaF_2 on glass but are modestly close to those values.

Figure 27 shows $w(L,t)$ calculated using Eq. (6) for the set III samples. The solid line is a fit to Eq. (11) resulting in $\beta=0.77\pm0.03$ with a prefactor of 0.16 ± 0.01. Figure 28

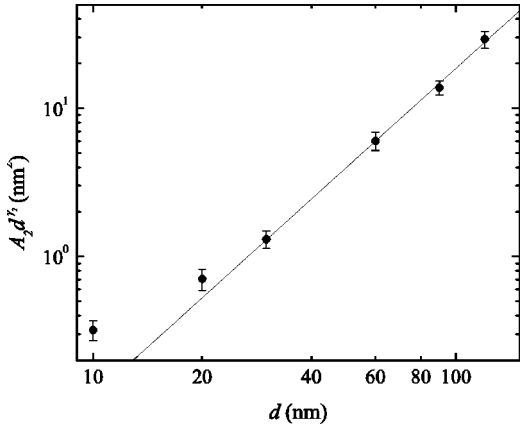

FIG. 26. The prefactors determined from a functional fit of the form $A_2\ell^{\gamma_2}$ applied to $C_2(\ell)$ for the gold plated substrates. The result is ad^b, where in this case, $a=0.0007\pm0.0001$ and $b=2.21\pm0.06$.

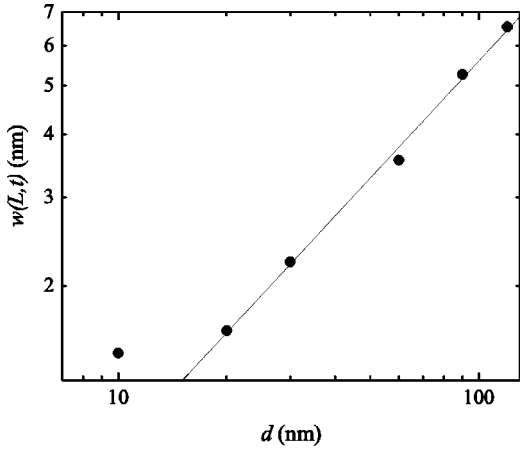

FIG. 27. $w(L,t)$ vs d on a log-log scale for the CaF_2 on gold-plated glass samples (set III). The solid line is a fit to Eq. (11) excluding the $d=10$-nm point, resulting in $\beta=0.77\pm0.03$.

shows $C_2(\infty)$ as function of d. The data were fit to Eq. (14) resulting in $\beta=0.78\pm0.03$ which is in agreement with value obtained from Fig. 27. The resulting prefactor was 0.05 ± 0.01. The point corresponding to $d=10$ nm does not follow the trend and was not included in either of the fits. The values of β found for the set III samples are in agreement with the value found for the CaF_2 on glass samples. The prefactors are also in agreement with the values found on glass for $w(L,t)$ and $C_2(\infty)$. Further, we have plotted H_q vs q for set III in Fig. 29 and again the data show similar behavior to the set I and II data. Only one region of power-law scaling was seen in the nearest neighbor height difference probability distribution for large δ. This is consistent with the results of the sets I and II substrates for this regime of d.

Figures 25, 26, and 29 indicate that there is a crossover from the gold film behavior to that seen in the CaF_2 films deposited directly on glass that occurs in the vicinity of $d \leqslant 20$ nm. The $d=10$-nm sample is in the middle of the crossover regime and therefore does not follow the trend of the higher d samples. This rapid crossover from the properties of

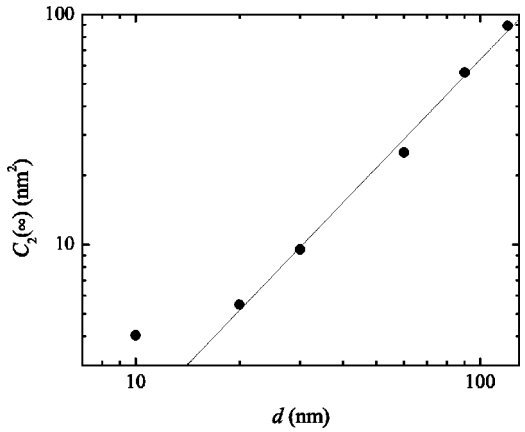

FIG. 28. $C_2(\infty)$ vs d on a log-log scale for the CaF_2 on gold-plated glass samples (set III). The solid line is a fit to Eq. (14) excluding the $d=10$-nm point, resulting in $\beta=0.78\pm0.03$.

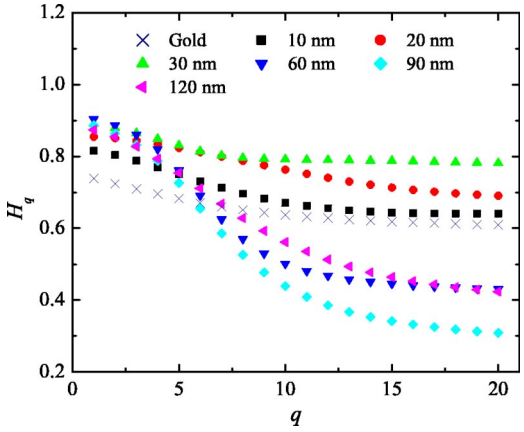

FIG. 29. H_q vs q for the set III samples. The numbers in the legend refer to the thickness of the CaF_2 film d.

the gold film to those seen in CaF_2 on glass substrates indicates that scaling properties of the CaF_2 films are not due to the initial conditions of the film growth, but rather are due to the CaF_2 itself. Therefore it is reasonable to conclude that power-law noise behavior is not due to initial conditions, but is caused by some other mechanism during the growth of the film. The possible source of the power law we observe noise is apparently qualitatively different than in the experiments where this type of noise was seen in $1+1$ dimensions. In those experiments [39–41] the power-law noise was observed in the presence of quenched noise. Our surfaces do not grow in the presence of quenched noise and it appears that the effect of the initial condition is quickly washed out.

E. Similarities with simulations in 1+1 dimensions

Finally, it is somewhat amusing to compare our experimental results in $2+1$ dimensions to several numerical studies that have been done in $1+1$ dimensions. First, we point out that the behavior of the skewness is similar to what has been seen in simulations for different models. Admittedly the data are noisy, but nonetheless the trend is that for small values of d, m_3 is close to zero and then decreases to $|m_3| \sim 0.3-0.5$, after which it increases to zero. This trend is similar to the skewness of the height distribution of several numerical studies investigating interface growth in $1+1$ dimensions [49,50]. It is also interesting to compare our porosity of the CaF_2 films on the smoother surface of glass with the model used to derive Eq. (23) . The numerical simulations done by Lam and Sander [44] with power-law noise in $1+1$ dimensions resulted in an aggregate with many embedded voids resulting from the rare noise events. Due to the relatively large measured porosity of our CaF_2 films on glass, we expect that voids also exist in the bulk of our films. Using the results of their simulations, Lam and Sander report for various values of μ the saturated velocity, defined as the mean of the deposit height divided by the number of layers of particles. This definition fits in with our definition of porosity [see Eq. (5)] and is in fact roughly equivalent to the slope of the line in Fig. 8, $(1-\phi)^{-1}=1.85\pm0.02$. The velocity is essentially independent of system size in the model. Tak-

ing into consideration the model is in $1+1$ dimensions, and that our surfaces have yet to saturate, for our value of μ we estimate a value for the velocity from Fig. 3 in Ref. [44] of roughly 1.9 ± 0.2, in agreement with our value obtained from the porosity.

V. CONCLUSIONS

We have investigated rough CaF_2 surfaces with film coverages spanning an order of magnitude using AFM and profilometer measurements. Our results indicate that the structures on the surface increase in height and width as the film thickness is increased. Our results are in qualitative agreement and modest quantitative agreement with other results. In addition, we have reported the increase in surface area, as seen by AFM, due to roughness, which increases with film thickness. We have also measured the porosity of the films, which we have found to be constant over the entire range of film thicknesses studied.

We have provided evidence consistent with the presence of a power-law-distributed noise spectrum resulting in the rough surface of vacuum deposited CaF_2. This is brought to light through the measurement of the multifractal spectra, the measurement of the distribution of nearest neighbor height differences, and the measurement of the critical exponents, all which give consistent results for the exponent in the noise distribution to be $\mu+1 \approx 4.6$. In addition, the set III data indicate that effects due to the initial conditions do not persist for large d. How this power-law-distributed noise is physically manifested is not known, nor is the direct physically significance of μ. In addition we have pointed out several similarities between our data and simulations done on a variety of other systems in $1+1$ dimensions, where direct comparisons cannot be made.

ACKNOWLEDGMENTS

We thank K. J. Thompson for assistance with sample fabrication and data collection. This work was supported by the National Science Foundation under Grant Nos. DMR-0138009 and DMR-0213695 (MRSEC) and also by research trust funds administered at the University of Massachusetts Amherst.

[1] J. L. Stanford, J. Opt. Soc. Am. **60**, 49 (1970).
[2] A. J. Braundmeier, Jr. and E. T. Arakawa, J. Phys. Chem. Solids **35**, 517 (1974).
[3] D.-L. Hornauer, Opt. Commun. **16**, 76 (1976).
[4] R. Orlowski, P. Urner, and D.-L. Hornauer, Surf. Sci. **82**, 69 (1979).
[5] S. O. Sari, D. K. Cohen, and D. Scherkoske, Phys. Rev. B **21**, 2162 (1980).
[6] G. H. Ames, D. G. Hall, and A. J. Braundmeier, Jr., Opt. Commun. **43**, 247 (1982).
[7] G. Rasigni, F. Varnier, J. P. Palmari, N. Mayani, and M. Rasigni, Opt. Commun. **46**, 294 (1983).
[8] F. Varnier, N. Mayani, and G. Rasigni, Appl. Opt. **28**, 127 (1989).
[9] D. R. Luhman and R. B. Hallock, J. Low Temp. Phys. (to be published).
[10] A.-L. Barabási and H. E. Stanley, *Fractal Concepts in Surface Growth* (Cambridge University Press, New York, 1995).
[11] T. Halpin-Healy and Y.-C. ZhangPhys. Rep. **254**, 215 (1995).
[12] M. Marsili, A. Maritan, F. Toigo, and J. R. Banavar, Rev. Mod. Phys. **68**, 963 (1996).
[13] J. Krug, Adv. Phys. **46**, 1391997.
[14] F. Varnier, C. Dussert, G. Rasigni, M. Rasigni, and A. Llebaria, J. Vac. Sci. Technol. A **6**, 1627 (1988).
[15] D. R. Luhman and R. B. Hallock, Phys. Rev. Lett. **92**, 256102 (2004).
[16] D. R. Luhman and R. B. Hallock, J. Low Temp. Phys. **134**, 245 (2004).
[17] J. C. Herrmann and R. B. Hallock, Phys. Rev. B **68**, 224510 (2003).
[18] Model SM-8 from R.D. Mathis Company, P.O. Box 92916, Long Beach, CA 90809.
[19] http://mathworld.wolfram.com/StatisticalCorrelation.html
[20] G. Rasigni, F. Varnier, M. Rasigni, and J. P. Palmari, J. Opt. Soc. Am. **73**, 222 (1983).
[21] F. Family and T. Vicsek, J. Phys. A **18**, L75 (1985).
[22] A. Iraji zad, G. Kavei, M. Reza Rahimi Tabar, and S. M. Vaez Allaei, J. Phys.: Condens. Matter **15**, 1889 (2003).
[23] H.-N. Yang, Y.-P. Zhao, G.-C. Wang, and T.-M. Lu, Phys. Rev. Lett. **76**, 3774 (1996).
[24] J. M. Gómez-Rodriguez, A. M. Baró, and R. C. Salvarezza, J. Vac. Sci. Technol. B **9**, 495 (1991); P. Herrasti, P. Ocón, L. Vázquez, R. C. Salvarezza, J. M. Vara, and A. J. Arvia, Phys. Rev. A **45**, 7440 (1992).
[25] A.-L. Barabási and T. Vicsek, Phys. Rev. A **44**, 2730 (1991).
[26] It has been pointed out in the literature [27] that the use of statistical error in the determination of the uncertainty of α underestimates the true error. The appropriateness of the direct applicability of these results to our values is not clear. Accordingly, we use our results as stated but do attempt to quantify this error for our system by reporting a range values of α for each substrate (see Table I).
[27] C. Castelnovo, A. Podestà, P. Piseri, and P. Milani, Phys. Rev. E **65**, 021601 (2002).
[28] H.-N. Yang, Y.-P. Zhao, A. Chan, T.-M. Lu, and G.-C. Wang, Phys. Rev. B **56**, 4224 (1997).
[29] M. Kardar, G. Parisi, and Y.-C. Zhang, Phys. Rev. Lett. **56**, 889 (1986).
[30] P. Meakin, P. Ramanlal, L. M. Sander, and R. C. Ball, Phys. Rev. A **34**, 5091 (1986).
[31] J. Krug, Phys. Rev. A **36**, 5465 (1987).
[32] E. Medina, T. Hwa, M. Kardar, and Y.-C Zhang, Phys. Rev. A **39**, 3053 (1989).
[33] Y.-C. Zhang, J. Phys. (Paris) **51**, 2129 (1990).
[34] Y.-C. Zhang, Physica A **170**, 1 (1990).
[35] J. Krug, J. Phys. I **1**, 9 (1991).

[36] C.-H. Lam and L. M. Sander, Phys. Rev. Lett. **69**, 3338 (1992).
[37] C.-H. Lam and L. M. Sander, Phys. Rev. E **48**, 979 (1993).
[38] S. V. Buldyrev, S. Havlin, J. Kertész, H. E. Stanley, and T. Vicsek, Phys. Rev. A **43**, 7113 (1991).
[39] V. K. Horváth, F. Family, and T. Vicsek, Phys. Rev. Lett. **67**, 3207 (1991).
[40] M. Myllys, J. Maunuksela, M. Alava, T. Ala-Nissila, and J. Timonen, Phys. Rev. Lett. **84**, 1946 (2001).
[41] M. Myllys, J. Maunuksela, M. Alava, T. Ala-Nissila, J. Merikoski, and J. Timonen, Phys. Rev. E **64**, 036101 (2001).
[42] R. Bourbonnais, J. Kertèsz, and D. E Wolf, J. Phys. II **1**, 493 (1991).
[43] A.-L. Barabási, R. Bourbonnais, M. Jensen, J. Kertèsz, T. Vicsek, and Y.-C Zhang, Phys. Rev. A **45**, R6951 (1992).
[44] C.-H. Lam and L. M. Sander, J. Phys. A **25**, L135 (1992).
[45] H. Katsuragi and H. Honjo, Phys. Rev. E **67**, 011601 (2003).
[46] Z. Csahók, K. Honda, E. Somfai, M. Vicsek, and T. Vicsek, Physica A **200**, 136 (1993).
[47] V. K. Horáth, F. Family, and T. Vicseck, J. Phys. A **24**, L25 (1991).
[48] C. Tang, S. Alexander, and R. Bruinsma, Phys. Rev. Lett. **64**, 772 (1990).
[49] D. E. Wolf, J. Phys. A **20**, 1251 (1987).
[50] J. Krug, P. Meakin, and T. Halpin-Healy, Phys. Rev. A **45**, 638 (1992).